

Topographic and stochastic influences on pāhoehoe lava lobe emplacement

Christopher W. Hamilton^{1,2}, Lori S. Glaze¹, Mike R. James³, and Stephen M. Baloga⁴

¹ Planetary Geodynamics Laboratory, NASA Goddard Space Flight Center, Greenbelt, MD, 20771, USA, christopher.hamilton@nasa.gov.

² Department of Astronomy, University of Maryland, College Park, MD, USA.

³ Lancaster Environment Centre, Lancaster University, Lancaster, UK.

⁴ Proxemy Research, Laytonsville, MD, USA

Abstract

A detailed understanding of pāhoehoe emplacement is necessary for developing accurate models of flow field development, assessing hazards, and interpreting the significance of lava morphology on Earth and other planetary surfaces. Active pāhoehoe lobes on Kīlauea Volcano, Hawai‘i, were examined on 21–26 February 2006 using oblique time-series stereo-photogrammetry and differential global positioning system (DGPS) measurements. During this time, the local discharge rate for peripheral lava lobes was generally constant at $0.0061 \pm 0.0019 \text{ m}^3/\text{s}$, but the areal coverage rate of the lobes exhibited a periodic increase every 4.13 ± 0.64 minutes. This periodicity is attributed to the time required for the pressure within the liquid lava core to exceed the cooling-induced strength of its margins. The pāhoehoe flow advanced through a series of down-slope and cross-slope breakouts, which began as ~ 0.2 m-thick units (i.e., toes) that coalesced and inflated to become approximately meter-thick lobes. The lobes were thickest above the lowest points of the initial topography and above shallow to reverse-

facing slopes, defined relative to the local flow direction. The flow path was typically controlled by high-standing topography, with the zone directly adjacent to the final lobe margin having an average relief that was a few centimeters higher than the lava-inundated region. This suggests that toe-scale topography can, at least temporarily, exert strong controls on pāhoehoe flow paths by impeding the lateral spreading of the lobe. Observed cycles of enhanced areal spreading and inflated lobe morphology are also explored using a model that considers the statistical likelihood of sequential breakouts from active flow margins and the effects of topographic barriers.

1. Introduction

Basalt is the most common rock type on the surface of terrestrial bodies throughout the solar system and—by total volume and areal coverage—pāhoehoe flows are the most abundant form of basaltic lava in subaerial and submarine environments on Earth (Self et al., 1994, 1998). Pāhoehoe flow fields are composed of flows, lobes, and toes, which represent a continuum of lava emplacement scales, with toes being the smallest elements. Pāhoehoe flows commonly advance as toes break out along lobe margins (Hon et al., 1994; Crown and Baloga, 1999; Hoblitt et al., 2012). These new toes quickly cool and develop a rheological gradient that includes an inferred three-part structure composed of a brittle outer crust, underlying viscoelastic layer, and inner molten core (Hon et al., 1994). As toes develop sufficient strength to retain incoming lava, they can pressurize, coalesce, and inflate to form lobes that are interconnected with other portions of the flow through internal fluid pathways (Walker, 1991, 2009). The evolution of these pathways can vary considerably (Kauahikaua et al., 1998), but the initial

47 emplacement of pāhoehoe flow fronts can influence the subsequent development of the
48 flow. Consequently, a detailed understanding of processes operating on the scale of toes
49 and lobes can provide important information for modeling aspects of flow field
50 development, assessing hazards, and interpreting the significance of lava flow
51 morphology on Earth and other planetary bodies (Peitersen and Crown, 2000; Byrnes and
52 Crown, 2001).

53 Hon et al. (1994) suggest that “microtopography” (i.e., tens of centimeters relief),
54 herein termed “toe-scale topography”, can strongly affect the emplacement of pāhoehoe
55 lava flows that reach a final inflated thickness of several meters. Previous studies have
56 attempted to determine the relationship between topography and pāhoehoe emplacement
57 (Crown and Balgoa, 1999; Peitersen and Crown, 2000; Byrnes and Crown, 2001), but
58 these studies have been unable to quantify the effects of toe-scale topography at the flow
59 front due to data resolution limitations. Here, oblique digital photogrammetry and
60 Differential Global Positioning System (DGPS) measurements are combined to quantify
61 key physical parameters involved in pāhoehoe flow advance through development of toes
62 and lobes, which constitute the fundamental building blocks of all pāhoehoe flows
63 (Walker, 1991; Self et al., 1996, 1998; Thordarson and Self, 1998). These field
64 observations are also used to inform and constrain a new stochastic model that describes
65 pāhoehoe lobe emplacement in terms of a balance between random and non-random
66 processes.

68 2. Background

Pāhoehoe flow fields exhibit a multitude of branching events at several scales (Crown and Baloga, 1999) and include self-similar morphologies (Bruno et al., 1994) that enable local observations to be used to understand larger aspects of flow fields and their emplacement. However, these patterns are complicated and irregular because of the influence of stochastic processes operating on multiple scales (Kilburn, 1996). This makes it important to identify the scales over which recurring processes and structures combine to form the overall pattern of a pāhoehoe flow field. Understanding how eruption parameters, deterministic factors, and random influences affect the emplacement and modification of pāhoehoe flows, also makes it possible to develop improved probabilistic models to describe likely patterns of flow growth (Glaze and Baloga, 2013). This study examines active pāhoehoe lava lobes on Kīlauea Volcano, Hawai‘i, to characterize the effects of toe-scale topography on flow emplacement and identify key parameters needed to model statistical aspects of the process.

Pāhoehoe flows grow through a combination of areal spreading and inflation, with new toes breaking out along lobe margins and quickly cooling by radiation (Hon et al., 1994; Keszthelyi and Denlinger, 1996; Harris et al., 2007a, 2013). Once a thin skin develops on the surface of the new toes, cooling becomes increasingly dominated by conduction (Castruccio et al., 2013). The crust also helps to retain incoming lava, which slows the advance of the new toes as their internal pressure decreases relative to the increasing confining strength of the growing crust (Hon et al., 1994). Given a constant influx of lava, this leads to a reduction in the areal coverage rate of the toes and an increase in the rate of inflation. Inflation will then continue to dominate the emplacement process until the internal pressurization of the lobe reaches a threshold required to rupture

the flow margins and initiate a new cycle of enhanced areal spreading (Hoblitt et al., 2012).

Within an active pāhoehoe flow, internal connections between numerous lobes can form extensive lava pathways (Kauahikaua et al., 1998). Preferred pathways within these lava networks tend to concentrate in existing topographic lows and may develop into a tube-system as the surrounding flow cools and stagnates. This allows pāhoehoe flows to advance great distances by transporting lava to the flow front through thermally insulated pathways that can reduce cooling rates to only 0.5–1.0°C/km (Helz et al., 1991). As lava is distributed from a master pathway into peripheral lobes and toes, the local discharge rates will progressively decrease with each branch in the system. Local discharge rates may therefore be constant over short periods of time (Hon et al., 1994), but are expected to evolve as the lobes at the former flow front are incorporated into the growing body of the lava transport system. In this study, lobes along the periphery of a low discharge pāhoehoe flow are examined to explore flow front emplacement processes and inflation.

3. Study Area

The Prince Kūhiō Kalanianaʻole (PKK) flow was erupted from Puʻu ʻŌʻō on Kīlauea Volcano, Hawaiʻi, from March 2004 to June 2007 (Fig. 1). Active margins along the flow were examined in the field between 21–26 February 2006. During this time, lava from Puʻu ʻŌʻō was primarily transferred through an established tube system that reached the ocean (Koeppen et al., 2013). However, during February 2006, the master tube-system also fed a series of small surface flows located ~7 km south of Puʻu ʻŌʻō. Harris

et al. (2007a) referred to this portion of the PKK flow as the “Hook flow”. Field observations and thermal imagery were used to establish that this flow exhibited breakouts of S-type pāhoehoe (Wilmoth and Walker, 1993) from three small flows on 21 February. However, by 23 February, the activity had dwindled to the distal margin of just one flow. Waning activity was also evidenced by a decrease in maximum core temperature from 1141°C on 21 February, to 1131°C on 23 February, and a decrease in areal coverage rate from $\sim 0.22 \text{ m}^2/\text{s}$ on February 22 to $\sim 0.03 \text{ m}^2/\text{s}$ on 23 February (Harris et al., 2007a). Additionally, there was a corresponding decrease in discharge rate feeding small surface flows, from $\sim 0.14 \text{ m}^3/\text{s}$ on February 22 to $\sim 0.03 \text{ m}^3/\text{s}$ on 23 February (Harris et al., 2007a). These surface flows stagnated on February 24. Measurements reported in this study were made contemporaneously with the observations of Harris et al. (2007a), who used thermal-image chronometry to establish broad relations among cooling, discharge rate, and areal coverage rates for the whole flow.

To place the local discharge rates discussed within this study into a broader context, the Pu‘u ‘Ō‘ō-Kupaianaha eruption began erupting in Kīlauea Volcano’s East Rift Zone (ERZ) in January 3, 1983, and between 1983 and 2002 its time-averaged discharge rate (Harris et al., 2007b) was $\sim 3.81 \text{ m}^3/\text{s}$ dense-rock-equivalent lava (Heliker and Mattox, 2003). However, the Pu‘u ‘Ō‘ō-Kupaianaha eruption has undergone numerous changes throughout its history (Heliker and Mattox, 2003) and in 2003–2007 the magma supply rate to the ERZ increased significantly during a mantle-derived surge to Kīlauea Volcano (Poland et al., 2012). During this time, the magma supply to Kīlauea Volcano increased by a factor of two (Poland et al., 2012). By 2005 the supply rate to the ERZ increased to $\sim 5.11 \text{ m}^3/\text{s}$ (Poland et al., 2012) and so at the time of the field campaign

in February 2006, effusion rates from Pu‘u ‘Ō‘ō were probably higher than the long-term average. Tilt meter records from the Hawaiian Volcano Observatory’s Pu‘u ‘Ō‘ō cone station also show that there was an oscillatory pattern of inflation and deflation between 21–26 February 2006 (Orr, 2011). This pattern began with an inflation event on 21 February, which was followed by gradual deflation over the next five days through a series of smaller tilt cycles (Tim Orr, personal communication, 2013). Orr (2011) showed that these tilt cycles were associated with fluctuations in lava discharge through the tube system and may have contributed to the observed breakouts from the master tube. Discharge rates associated with the small surface flows examined within this study were therefore much lower than for the concurrently active PKK tube and the eruption as a whole.

4. Methods of Digital Terrain Modeling

To quantify aspects of the pāhoehoe emplacement processes, two complementary methods were employed. First, time-series oblique stereo-imaging and photogrammetry (Robson and James, 2007) were used to determine the changing geometric properties of an active lava lobe, herein referred to as Lobe A. Second, Differential Global Positioning System (DGPS) measurements of topography before and after the emplacement of a second pāhoehoe lobe (Lobe B) were used to assess the relationship between initial topography and final lobe morphology. Lobes A and B were located along the same lava pathway system, with Lobe B located ~10 m directly down-flow of Lobe A.

Time series stereo-image pairs of Lobe A were acquired on 23 February using two synchronized tripod-mounted digital Single Lens Reflex cameras (6 mega-pixel

Canon EOS 300D), which collected image pairs every minute over a duration of 35 minutes (Robson and James, 2007). The cameras were mounted approximately one meter apart and had pre-calibrated, fixed-focus 28 mm lenses. Photogrammetric control was provided using spherical targets (0.25 mm in diameter) with positions determined by DGPS measurements. The analysis was carried out using Vision Measurement System (Robson and Shortis, <http://www.geomsoft.com>) with image matching by the GOTCHA dense matching algorithm (Gruen, 1985; Day and Muller, 1989; Otto and Chau, 1989). A typical stereopair provided topographic point cloud data with positional precisions of 25, 65 and 20 mm in easting (x), northing (y), and elevation (z), respectively. To quantify surface changes, these point cloud data were gridded in Surfer using a Kriging algorithm over a 0.1 m/pixel x - y grid. The data were then imported into ArcGIS.

For Lobe B, x , y , and z coordinates for topographic surfaces were acquired before (23 February) and after lava emplacement. Post-emplacement surveys were performed on 24–26 February; however, no changes were observed after 24 February and so data from these three surveys were combined together. Data were collected at a sampling rate of 0.5 seconds using two Ashtech Z-Xtreme DGPS receivers—one operating in kinematic mode and the other as a static base-station. These data were post-processed using Ashtech Solutions 2.60 with differential, L1/L2 (1575.42 MHz/1227.60 MHz) frequency correction for ionospheric delay error, and International Global Navigation Satellite System Service Standard Product 3 precise orbit file corrections. Resulting data points were filtered to remove measurements with more than 0.05 m residual accuracy error. On volcanic terrains, Hamilton et al. (2010) estimate the vertical precision of single traverse kinematic DGPS surveys to be ± 0.08 m, and double traverses being ± 0.06 m, with

horizontal precision being better than the vertical measurements. Most gridded cells in this dataset contain multiple DGPS observations and should have a vertical precision of ± 0.06 m. The resulting datasets for the initial and final topography include 14,618 and 20,585 records, respectively. To avoid spatial aliasing and to eliminate redundant data, the BLOCKMODE function in Generic Mapping Tools (GMT; Wessel and Smith, 1991) was used to average z within each pixel. Filtered x , y , and z , data were then interpolated using NEARNEIGHBOR in GMT to form a 0.1 m/pixel x - y grid.

5. Time Series Observations of Pāhoehoe Lobe Emplacement

Stereogrammetric point clouds and interpolated Digital Terrain Models (DTMs) were used to identify and digitize the active margins of Lobe A at 1-minute intervals (Fig. 2). These areal spreading maps show that the lava lobe grew by a series of breakouts that broadly fit into two categories: narrow (0.2–0.6 m-wide) toes that grew preferentially down-slope and broad (1.4–3.5 m-wide) breakouts that formed along the sides of the lobe, nearly perpendicular to the down flow axis (Figs. 3 and 4). Initial toe thicknesses were typically ~ 0.2 m and, during the 35 minute period of observation, they inflated to a maximum thickness of ~ 1.1 m, with most toes inflating to half their final thickness within 10 minutes. Within the first minute of emplacement toes generally extended ~ 0.2 m, with a range of 0.05 to 0.55 m. After 28 minutes, the active flow margin began to exit the field of view of the stereo cameras and toe lengths could not be accurately constrained.

The mean local discharge rate measured at Lobe A over the first 19 minutes was $0.0061 \pm 0.0019 \text{ m}^3/\text{s}$ ($N = 19$, Fig. 5a). Note that all uncertainties in this study are reported at 1 standard deviation, σ , unless otherwise noted. Standard deviation describes

how much variation there is from the mean, whereas standard error on the mean, σ_μ , provides a measure of how well the mean is known based on the number of data points, N , used in the calculation. We therefore provide N as well as σ to enable the calculation of $\sigma_\mu = \sigma/\sqrt{N}$. After 35 minutes, the lobe covered a new area of 11.7 m² and achieved a cumulative volume of 10.4 m³.

This local discharge rate was remarkably constant during the observation period, except for the interval between 19 and 24 minutes, when it decreased by nearly a factor of four. During this interval, the lobe experienced little inflation and generally lower than average areal spreading rates (Fig. 5a), which may have been due to breakouts occurring outside the field of view. At 24 minutes, the local discharge rate of 0.0061 m³/s resumed, but after 28 minutes, the measured rate of volume change gradually decreased as the active flow front began to exit the field of view of the stereo-cameras. The mean areal coverage rate was 0.0055 ± 0.0038 m²/s ($N = 35$). The areal coverage exhibits a periodicity with peaks ~3 times greater than the mean (Fig. 5b) and a period of 4.13 ± 0.64 minutes ($N = 8$). During each cycle of areal growth (measured from trough to trough in areal coverage rates shown in Fig. 5b), the lobe covers a new area of 1.59 ± 0.28 m² ($N = 7$).

Excess volume refers to the portion of a lava lobe that is not directly associated with its initial areal expansion. In this case, excess volume is defined as the volume change in the field of view per minute minus the change in area during that minute multiplied by the typical initial thickness of the new breakouts. The typical thickness of new breakouts from Lobe A was ~0.2 m, but may vary for other flows—generally scaling with local discharge rate (Self et al., 1998). Excess volume changes for Lobe A appears

to be weakly anti-correlated with its areal spreading rate. However, to quantify the degree of anti-correlation, the cross-correlation coefficient was calculated between the areal growth and excess volume. The correlation analysis was restricted to the first 19 minutes of observation when the volume flow rate feeding the lobe was relatively constant. The areal growth rate during this 19 minute period exhibits a slight overall increase over time (slope = $0.013 \text{ m}^2/\text{minute}$ and intercept = $0.206 \text{ m}^2/\text{minute}$), and therefore the trend was removed prior to analysis. After trend removal, the cross correlation coefficient, at lag = 0 (the measure of direct anti-correlation) is -0.22. The negative sign of this statistic indicates anti-correlation; however, the magnitude is well within the 90% confidence interval (± 0.34) indicating that the anti-correlation is very weak and not statistically significant at this level. This suggests that there may be a trade-off between areal spreading and inflation given an approximately constant lava supply, but that the relationship may be complicated by other factors. See Section 7.2 for further discussion.

6. Lava Thickness, Inflation, and the Effects of Topographic Relief on Pāhoehoe Lobe Emplacement

Topographic maps of the terrain before and after the emplacement of Lobe B are shown in Figure 6. Lava covered 111.83 m^2 within the DGPS survey region, with a total lobe volume of 59.45 m^3 . Forward Looking Infrared Radiometer (FLIR) measurements of the flow at 06:00 on 24 February 2006, revealed no anomalously hot pixels within the study region, which indicates that the flow terminated at least 5 hours before (Harris et al., 2007). Based on the time of the last field observations on 23 February, this constrains the emplacement duration to <8 hours. If the mean areal coverage and discharge rates

were similar for Lobes A and B, then the emplacement duration of Lobe B was likely between 2.6 and 5.2 hours.

Using the before and after DTMs (Figs. 6a and b), topographic profiles have been extracted down-slope (Fig. 7a) and cross-slope (Fig. 7b). The lava entered the study region from the north and the lobe grew to a length of ~18 m and a maximum width of 9.1 m. However, the distal part of the flow focused into a 4.3 m-wide topographic constriction before being bifurcated by a 1.0 m-high topographic obstacle into two smaller lobes that were 2.4 m and 4.0 m-wide. The profiles show that inflation of the lava tended to topographically invert the landscape, with the thickest portions of the lobe developing above topographic depressions and shallow to reverse-facing slopes, defined relative to the local flow direction. Thus, apparent barriers to the spreading of the flow are typically much smaller than the maximum height of the lobe and the thicker portions of the lobe appear confined by the thinner peripheral parts of the flow.

The thickness distribution of Lobe B (Fig. 6c) above the existing surface was calculated by taking the simple difference between the final and initial topography. This yields a mean lobe thickness of 0.57 ± 0.24 m, with a maximum of 1.21 m. However, simple topographic difference overestimates inflation because lobes are initially emplaced as toes with an initial thickness. Additionally, lava had to fill small closed depressions before thickening above the surrounding topography.

To account for the infilling of small topographic depressions, a new initial surface was created by smoothing the initial topography in a process that is analogous to tightly stretching a rubber sheet through the data. The smoothed surface was created using the GMT function SURFACE, which interpolates a grid using continuous curvature splines

in tension (Smith and Wessel, 1990). Specifically, SURFACE applies the Laplace transform (L) to the initial topography (z):

$$(1-T) L \times (L(z)) + T \times L(z) = 0. \quad [1]$$

Varying the tension factor T between 1 (i.e., the harmonic surface solution) and 0 (i.e., the minimum curvature solution) enables this data interpolation method to smooth the initial surface to different degrees. For instance, a grid produced with high tension ($T \rightarrow 1$) will suppress local maxima and minima by fitting an increasingly taut surface between the data constraints, whereas applying a looser tension factor ($T \rightarrow 0$) will produce a smooth polynomial function analogous to a flexed elastic plate that is anchored by the data (Smith and Wessel, 1990).

To constrain the inflated thickness of Lobe B, a smoothed local datum was fit to the initial topography using a T -value of 1. This removes high frequency oscillations in the topography, while preserving the overall shape of the terrain. Subtracting this surface from the final topography isolates the thickness of lava above the local datum and provides a better proxy for inflation than the simple difference map because it reduces the thickness contributions due to small basin infilling. Using this method, the mean thickness due to inflation was 0.34 ± 0.21 m ($N = 9614$), with a maximum of 1.00 m (Fig. 6d).

To isolate local relief within the initial topography, a second interpolated surface was created using Eq. (1) with $T = 0.25$. A loose tension factor of $T = 0.25$ is recommended for low-tension interpolations to suppress extraneous oscillations (i.e., minima and maxima) that can otherwise be generated within the $T = 0$ (i.e., end-member minimum curvature) solution (Wessel and Smith, <http://gmt.soest.hawaii.edu/>). The new

surface preserves more variations in the initial topography than the harmonic surface solution ($T = 1$) and was subtracted from the original initial topography to isolate high frequency changes in elevation (i.e., relief) above and below a new local datum centered on 0 m.

In the lava inundated region, the distribution of initial relief is unimodal with a mean of -0.02 ± 0.07 m ($N = 9614$ pixels; Fig. 8). For comparison, a 1-pixel buffer region was also defined around the outer extent of the lobe and, in this buffer region, the frequency distribution of relief had a mean of 0.00 ± 0.07 m ($N = 499$ pixels). However, relative to the lava inundated region, there are more pixels with a relief of 0.03 to 0.09 m and fewer pixels with a relief of -0.09 to -0.03 m (Fig. 8). This implies that there are systematically more high relief pixels bounding the pāhoehoe lava lobe than in the region that was inundated. Consequently, positive relief on the order of only a few centimeters may exert an important influence on bounding the extent of low-effusion-rate pāhoehoe flows.

Toe-scale topography (i.e., on the order of centimeters in this case) appears to influence the areal spreading of pāhoehoe lobes by blocking peripheral toes, which may then stagnate and help confine the interior portions of the flow. If the interior of the flow continues to be supplied by lava it may then inflate above the height of the surrounding barriers, thereby topographically inverting the landscape. Barriers to flow may therefore be much less than the final inflated thickness of a lobe. Based on observations of Lobe B, relief that is at least 15% of a toe's initial thickness may be significant in terms of affecting the path of low-discharge pāhoehoe lava lobes, but given sample-size-dependent restrictions on the optimum bin-size for the data (Stuges, 1926; Doane, 1976),

influences of even smaller variations in topography cannot be precluded. Obstacle heights affecting the path of higher local discharge rate flows may similarly scale with initial toe height.

7. Stochastic Modeling of Pāhoehoe Lobe Emplacement

7.1. Overview of the Model

Random effects strongly influence processes of pāhoehoe flow growth and pose a fundamental difficulty in developing models for their emplacement (Hon et al. 1994; Thordarson and Self, 1998; Keszthelyi et al., 1999; Crown and Baloga, 1999). Glaze and Baloga (2013) have recently developed a new simulation approach for modeling pāhoehoe emplacement that builds on the ideas presented in Baloga and Glaze (2003). This model is based on (1) conservation of lava volume and (2) prescribed stochastic rules for lava movements within a pāhoehoe lobe. This approach differs significantly from other models that treat lava emplacement as a gravity-driven viscous fluid flow on an inclined plane (e.g., Danes, 1972; Hulme, 1974; Baloga and Pieri, 1986; Baloga, 1987; Crisp and Baloga, 1990; Harris and Rowland, 2001; Rowland et al., 2004; Baloga and Glaze, 2008). The Glaze and Baloga (2013) model simulates the 3-Dimensional shape for pāhoehoe lobes as they evolve in time, subject to a wide variety of ambient and internal conditions and processes. Here, the new model is used to explore the effects of inflation on pāhoehoe lobes analogous to Lobes A and B.

The fundamental building block of the Glaze and Baloga (2013) model is the lava “parcel”. A “parcel” of lava is defined here as a volumetric unit sampled from a probability distribution of lava volumes that typically construct a pāhoehoe lobe. Thus

the smallest toe observed on the surface or along the margins of a pāhoehoe lobe represents a lava parcel volume from the small end of the distribution. However, larger toes may either represent a larger parcel volume, or may be comprised of multiple parcels.

A parcel is observable as a “toe” when it is permanently affixed at the surface or margin of a lobe. In the Glaze and Baloga (2013) model, lava parcels originate from a source region and are transported through fluid internal pathways. For the purposes of discussion here, the model assumes a constant parcel size for all parcels. Crown and Baloga (1999) measured dimensions of hundreds of toes and their mean thickness is very well constrained at ~ 0.20 cm, (0.19 ± 0.08 m, $N = 448$). Based on the geometric mean toe sizes measured by Crown and Baloga (1999), the parcel volume is assumed to be 0.09 m^3 (Glaze and Baloga, 2013). Assuming a square x - y grid and a typical parcel thickness of 0.2 m—comparable to the observed initial thickness of toes in our study area—the corresponding cell spacing is 0.67 m, with a parcel area of 0.45 m^2 .

The Glaze and Baloga (2013) random simulation model begins with an initial source region (a single point, linear source, etc.), a constant supply of lava (i.e., one parcel per time step), and probabilistic rules governing where each parcel will be transferred and allocated. For example, in the most basic scenario of complete randomness, two random choices are made for each breakout. First, a parcel is randomly selected to be the source for the next parcel transfer. Second, a random selection is made to determine the orientation of the new parcel transfer relative to its source (i.e., North, South, East, or West). In the purely random case, every face of every parcel has an equal probability of being the source for the next parcel transfer. As various factors that

influence emplacement are examined (e.g., barriers, slope, etc.), different probabilistic rules are applied that determine where and when each parcel will be transferred.

7.2. Model Simulations of Areal Growth

Figure 9a shows a typical example of a completely random simulation involving 500 parcels. In this simulation, each transfer location and direction is chosen at random. Figure 10a (solid line) shows the corresponding cumulative area as a function of time step. However, Glaze and Baloga (2013) showed that topographic profiles of pahoehoe lobes are more consistent with simulations that include sequential breakouts at the margin. In this case, the momentum of new parcels breaking out from a lobe margin results in an increased probability that the next parcel will be transferred from the most recent parcel in the same direction. Figure 9b shows the influence of allowing sequential breakouts at the lobe margin on lobe morphology. Specifically, every time a new parcel is transferred to the margin (increasing the lobe area) probabilistic rules are used to determine whether 0, 1, or 2 extra parcels will be added at that location. For the simulation shown in Figure 9b, the probability of 0 additional parcels is $P(0) = 0.25$, of 1 additional parcel being added is $P(1) = 0.25$, and of 2 additional parcels is $P(2) = 0.5$. As expected, the cumulative area of the simulation that includes sequential breakouts at the margin rapidly diverges from the purely random simulation (Fig. 10a), exhibiting a steeper gradient and overall greater cumulative area. Although a general trend in the areal growth (m^2 per time step) is evident in both simulations shown in Figure 10a, the curves are irregular with periods where the area increases rapidly and periods where the area does not change at all. Also as expected, the rate of overall areal growth tapers off over

time as the number of available lava transfer locations along the margins decreases relative to the total area of the lobe.

The Glaze and Baloga (2013) simulation approach explicitly requires that lava parcels will either expand the area of the flow or contribute to inflation if they are allocated to the flow interior. This naturally results in a trade-off between areal growth and interior lobe inflation similar to the pattern observed during the emplacement of Lobe A. The natural periodicity of the areal growth rate in the simulated lobes is illustrated by the solid line in Figure 10b. Also shown in Figure 10b is the excess volume, which was defined in Section 5 as the volume in addition to what is directly associated with the change in lobe area because all breakouts will be emplaced with some initial thickness. For the simulated data, the definition of excess volume results in a periodic behavior that exactly mirrors the areal growth (i.e., perfect anti-correlation). This suggests that the weak anti-correlation shown in Figure 5b may be relevant, but also indicates that other processes are present in the field that have not yet been accounted for by the model. Also in the field example, there was a period of anomalously low average lava flux between 20–23 minutes, which coincided with a period of negative excess volume change. This indicates that areal spreading can also be accommodated by the depletion of lava stored within the parent lobe, rather than always being related to a simple balance between pressurization and confining strength under conditions of constant lava supply. Future studies would therefore benefit from longer time-series observations of multiple active lava lobes to further explore the statistical significance of the relationship between areal spreading and inflation.

7.3. Comparisons Between Model Simulations and Observations

Given the measured volume of Lobe A and typical parcel volume of 0.09 m^3 , Lobe A would include ~ 117 parcels. The simulation of a lobe composed of 117 parcels begins with a 1×7 cell linear source region trending East-West (depicted as the gray shaded region in Figure 11a crossing through the mid-point of the array). This source region, with one parcel in each of the seven cells, is approximately equivalent to the initial length of Lobe A (i.e., $\sim 4.69 \text{ m}$; see Fig. 4a). The model also includes two parallel barriers located at ± 3 cells along the North-South axis. The barriers are considered transitional zones in which the advancing lava enters, but becomes blocked, thereby reflecting the lava parcel back toward the interior of the flow. The distance between these barriers is 4.69 m (including the barrier cells as well), which corresponds to the topographically-bounded maximum width of Lobe A. The probabilities of sequentially adding 0, 1, or 2 extra parcels from an existing flow margin are $P(0) = P(1) = 0.25$, and $P(2) = 0.5$.

One cannot expect any specific realization of the stochastic model to exactly reproduce the morphology of an observed lava lobe, but characteristics of the simulated lobes are broadly consistent with the morphology of Lobe A. Figure 11b shows examples of topographic profiles taken perpendicular to the flow direction through the simulated lobes averaged over 10, 20, 30, and 60 realizations. These examples demonstrate that there are stochastic variations between simulations, but also persistent morphological characteristics. For example, the simulated lobes are thickest in the middle (i.e., along the axis of the linear source region) with maximum heights that are consistent with those observed for Lobe A. The models also exhibit the effects of lava confinement along lobe

margins due to lava parcels being reflected back toward the interior of the flow. Plan views of the simulated lobes (e.g., Figs. 9a and 9b) also show irregular margins and thickness variations that are typical of inflated pāhoehoe lobes.

8. Discussion

8.1. Relationships between Pāhoehoe Breakouts and Inflation

Pāhoehoe breakouts will be emplaced with some initial thickness and then grow through a process of inflation. This inflation process includes two dominant components: thickening of the molten core and thickening of the crust (Hon et al., 1994), with the crust consisting of both a brittle outer layer and underlying viscoelastic layer. After an initial chilled margin forms around a new toe, it will retain incoming lava and inflate as its molten core thickens to equalize the pressure with other connected portions of the fluid lava pathway. During the early stages of emplacement, the rate of core thickening will greatly exceed the rate of crustal thickening (Hon et al., 1994), but as the fluid interior achieves its equilibrium thickness, inflation will be increasingly dominated by the process of crustal growth (Cashman and Kauahikaua, 1997).

Two conditions must be met for the upper crust to continue to accrete new material and contribute to inflation. First, there must be a continuous influx of new lava through the molten core and, second, there must be physical coupling of the molten core to the upper crust (Kauahikaua et al., 1998). If the flow of lava through the core stagnates then the lava will cool *in situ* and will not increase the flow's total thickness.

Additionally, if the molten core partially drains and decouples from the upper crust then new material will not be added to the base of the surface layer and the crust may even

subside and “deflate” (Kauahikaua et al., 1998). Cooling histories inferred from the thicknesses of the upper brittle and viscoelastic layers (Hon et al., 1994) therefore provide an estimate of the time that a lava pathway flowed at full capacity, but not necessarily the total duration of emplacement if the core of the flow and the upper crust were decoupled. In some cases, the molten core of a flow can also undergo cycles of pressurization related to changes in the local discharge rate (Orr, 2011). This can lead to variations in molten core pressure that induce cycles of surface disruption and subsidence, thereby producing a range of surface textures that include slabbly pāhoehoe, rubbly pāhoehoe, and shatter rings.

Initial cooling can strengthen the margins of a lava flow (Castruccio et al., 2013), but the process is complicated by the development of numerous cooling fractures. These fractures will mechanically weaken the outer brittle crust and make the underlying viscoelastic layer more important in terms of governing the overall confining strength of the flow. The frequency of breakouts will therefore depend on the balance between the combined strength of the brittle and viscoelastic layers relative to the pressure within the molten core (Hoblitt et al., 2012). If the internal pressure exceeds the confining strength of the flow’s outer layers, then the periphery of the flow will rupture and generate new breakouts that promote increased areal growth. In contrast, if the exterior of the flow does not rupture, it will pressurize and inflate through gradual deformation of the viscoelastic layer and opening of fractures in the overlying brittle crust.

In this study, peripheral lobes along the margins of the PKK flow on the flanks of Kīleaua Volcano, exhibited a generally constant local discharge rate (0.0061 ± 0.0019 m²/s). However, approximately every four minutes there was a significant increase in the

areal spreading rate. The observed periodicity in areal coverage may relate to the changing balance between the confining strength of the lava as it cools and strengthens, and the internal pressure within the core of the flow. This balance would give rise to an increased frequency of new breakouts when the core pressure exceeds the confining strength of the exterior. Enhanced areal spreading rates would then persist until the core pressure decreases below a critical threshold required to continuously rupture the active flow margin. As the rate of areal spreading decreases, continued influx of lava into the lobe would begin to re-pressurize its fluid core and perpetuate a new cycle. This process, operating on the scale of an individual lobe, is similar to what Hoblitt et al. (2012) have observed on the scale of an entire pāhoehoe flow, which demonstrates the self-similarity of the inflation mechanism over a range of scales.

8.2. Static and Dynamic Pressure Considerations

During early stages of pāhoehoe emplacement, the inflation process will be dominated by molten core thickening as the liquid interior of the flow moves toward an equilibrium thickness. However, there are multiple factors that can contribute to this equilibrium. Calculations generally assume a Bingham liquid rheology, with lava descending a slope as an unconfined laminar flow under the influence of gravity (Hulme, 1974; Dragoni et al., 1986; Castruccio et al., 2013). Within this scenario, the critical depth h_s required to induce down-slope flow will be

$$h_s = \sigma_0 / \rho g \sin(\beta), \quad [2]$$

where σ_0 is the flow's yield stress, ρ the flow's density, g is gravitational acceleration, and β is the underlying slope (see Eq. [14] in Hulme, 1974). However, such calculations

of a lava flow's equilibrium thickness will be complicated by cooling-induced changes in rheology and other factors that influence its internal pressure once the molten core is confined by a coherent crust. Several studies (e.g., Rossi and Gudmundsson, 1996; Anderson et al., 1999, 2012) have considered the “magmastatic” pressure (herein referred to as “hydrostatic” pressure) generated by fluid elevation changes along a hydrostatically connected pathway, as well as the pressure required to drive lava through pipe-like pathways and lift the crust. These models generally assume that the pathways (i.e., lava tubes) are cylindrical pipes with constant cross-sectional area, but the geometry of lava pathways can vary widely within a pāhoehoe flow (e.g., Guest et al., 1984; Kauahikaua et al., 1998; Self et al., 1998; Calvari and Pinkerton, 1999). This raises the possibility that changes in pathway geometry can introduce additional changes in lava core pressure due to dynamic processes.

These dynamic effects may be understood within the context of Bernoulli's principle, which describes the inverse relationship between fluid flow velocity and fluid pressure within incompressible laminar flows through a pipe (Resnick and Halliday, 1977; Batchelor, 1998). For lava moving within a system of combined pathways, changes in fluid core pressure could affect inflation rates by changing the magnitude of the stresses applied to the overlying crust. This may lead to increased inflation rates where the flow velocity decreases and the core pressure increases. Conversely, inflation rates would be lower where the flow velocity increases and the core pressure decreases. For otherwise equivalent lava flows through a pipe-like pathway, the most important controls on fluid velocity will be the pipe's cross-sectional area and underlying slope. In general, lava velocities will be relatively low where the flow pathway is broad and its cross-

sectional area is large and/or where it descends a shallow slope or encounters a reverse-facing slope. Alternatively, flow velocities will be higher when lava enters a narrow topographic constriction and/or descends a steeper slope. These scenarios are broadly consistent with the observed relationship between the initial topography and final morphology for Lobe B. In this case, maximum inflation was observed where the flow was the broadest and above shallow to reverse-facing slopes, whereas the least inflation was observed where the flow passed through narrow constrictions and descended steep slopes (Figs. 6 and 7). These observations support the viability of a conservation of energy approach to modeling the spatial variability of inflation and its relationship to emplacement processes. They also highlight the importance of including both fluid static and dynamic components in understanding core pressure and thickening during the early stages of pāhoehoe inflation. Early stage inflation processes related to core pressurization and thickening may also help to establish preferred pathways through the thickest parts of the flow, which would continue to preferentially inflate through crustal accretion if the pathways remain full. Continued crustal accretion and uplift must also be coupled with overpressurization of the molten core, which Cashman and Kauahikaua (1997) inferred from their observations of pāhoehoe crustal vesicularity profiles that exhibit decreased vesicle number density with depth.

9. Conclusions

The confining strength of a lava lobe depends strongly on the age distribution of its surfaces, with the youngest surfaces (i.e., sites of the most recent breakouts) being the weakest. Therefore, when new breakouts occur, growth tends to concentrate at these

localities. Otherwise, the next most likely location for a breakout to occur is from an older fractured surface overlying a still molten core. This process is treated with a stochastic model by introducing correlation with a probability distribution describing the preferential growth of the flow in the direction of new breakouts through sequential emplacement of lava parcels (i.e., toes) from that locality. Including correlated growth into the model also recreates observed periods of enhanced areal spreading and lobe morphologies.

Time-series data for Lobe A shows that periods of enhanced areal spreading roughly alternate with periods of increased excess volume change. For an approximately constant local discharge rate, this suggests that the volume of lava not utilized during the process of areal spreading can contribute to thickening through inflation. Trade-offs between areal spreading and inflation should be detectable in thermal infrared (e.g., FLIR) imagery, provided that a single lobe is isolated in the field of view. For instance, when the flow enters a period of above average areal spreading, newly exposed lava surfaces will radiate more thermal energy and will contribute to an increased frequency distribution of high temperature pixels within the field of view. As the flow shifts toward an inflation-dominated mode, older lava surfaces will cool dominantly by conduction rather than radiation (Hon et al., 1994), and this would shift the frequency distribution of temperatures toward lower values. Temperature distributions in FLIR data may therefore be used to identify patterns of pāhoehoe flow emplacement, such as periodicities in areal spreading rate and the trade-off with inflation. Statistical models of flow emplacement may be improved by coupling them with a cooling model to estimate the temperature distribution of the lava based on its emplacement age.

New toes are highly sensitive to subtle topographic irregularities and for low discharge rate flows may be deflected or stopped by obstacles measuring only a few centimeters in height. This process was observed during the emplacement of Lobe B and demonstrates that the final morphology of a lobe may inherit boundaries influenced by variations in the initial toe-scale topography that are orders of magnitude smaller than the flow's final thickness. Even though toes may be locally deflected or impeded by toe-scale topography, inflating pāhoehoe lobes may overcome local barriers through a combination of stochastic breakouts in down-flow and cross-flow directions that allow them to find and follow the maximum regional slope. These behaviors are described in the model by considering the sequential emplacement of new lava parcels (i.e., toes) from existing flow margins, with boundaries that reflect parcels back towards the interior of the flow.

Combining measurements of initial topography with time-series observations of active pāhoehoe lobes provides new insights into the growth of pāhoehoe flows. These observational constraints also help to improve statistical models of lava emplacement processes and better understand the relationship between areal expansion and inflation. This information is important for understanding how subtle topographic influences can be inherited by inflated lobes to develop preferred lava pathways that influence the overall development of a flow and for interpreting the emplacement history of pāhoehoe lava flows on Earth and other planetary surfaces.

Acknowledgments:

We thank Benjamin Brooks and the Pacific GPS facility for providing access to DGPS survey equipment and post-processing resources, Samuel Hulme for his assistance

598 *with GMT, Richard Herd for kindly providing DGPS data for photogrammetry control,*
599 *Andy Harris for his assistance in the field making contemporaneous FLIR observations,*
600 *Tim Orr for providing historical lava flow data shown in Figure 1, as well as Sarah*
601 *Fagents, Thorvaldur Thordarson, and Jacob Bleacher for many insightful discussions*
602 *relating to lava flow emplacement. Prof. S. Robson and Prof. J. P. Muller are thanked for*
603 *their ongoing support through provision of VMS and GOTCHA, respectively. Christopher*
604 *Kilburn and Jim Kauahikaua are sincerely thanked for their thorough and constructive*
605 *reviews. Field work was conducted in Hawaii Volcanoes National Park under Scientific*
606 *Research and Collecting Permit # HAVO-2006-SCI-0003. CWH was supported by an*
607 *appointment to the NASA Postdoctoral Program at the Goddard Space Flight Center,*
608 *administered by Oak Ridge Associated Universities through a contract with NASA. LSG*
609 *and SMB research was supported by the NASA Planetary Geology and Geophysics, and*
610 *Mars Data Analysis programs (LSG: 811073.02.01.04.44 and 203959.02.03.17.56; SMB:*
611 *NNX08AF16G and NNX10AP63G).*

References

- Anderson SW, Stofan ER, Smrekar SE, Guest JE, Wood B (1999) Pulsed inflation of pahoehoe lava flows: implications for flood basalt emplacement. *Earth Planet Sci Lett* 168:7–18
- Anderson SW, Smrekar SE, Stofan ER (2012) Tumulus development on lava flows: insights from observations of active tumuli and analysis of formation models. *Bull Volcanol* 74:931–946. doi:10.1007/s00445-012-0576-2
- Baloga S (1987) Lava flows as kinematic waves. *J Geophys Res* 92 (B9):9271–9279
- Baloga S, Pieri DC (1986) Time-dependent profiles of lava flows. *J Geophys Res* 91:9543–9552
- Baloga S, Glaze LS (2003) Pahoehoe transport as a correlated random walk. *J Geophys Res* 108:2031. doi:10.1029/2001JB001739
- Baloga S, Glaze LS (2008) Self-replication model for long channelized lava flows on the Mars plains. *J Geophys Res* 113:E05003. doi:10.1029/2007JE002954
- Batchelor GK (1980) *An introduction to fluid dynamics*. Cambridge Univ Press, New York, 615 p
- Bruno BC, Taylor GJ, Rowland SW, Baloga SM (1994) Quantifying the effect of rheology of lava-flow margins using fractal geometry. *Bull Volcanol* 56:193–206
- Byrnes JM, Crown DA (2001) Relationships between pahoehoe surface units, topography, and lava tubes at Mauna Ulu, Kilauea Volcano, Hawaii. *J Geophys Res* 106(B2):2139–2151

633 Byrnes JM, Ramsey MS, Crown DA (2004) Surface unit characterization of the Mauna
 634 Ulu flow field Kilauea Volcano, Hawai‘i, using integrated field and remote
 635 sensing analyses. *J Volcano Geotherm Res* 135:169–193
 636 Calvari S, Pinkerton H (1999) Lava tube morphology on Etna and evidence for lava flow
 637 emplacement mechanisms. *J Volcanol Geotherm Res* 90:263–280
 638 Cashman KV, Kauahikaua JP (1997) Reevaluation of vesicle distributions in basaltic lava
 639 flows. *Geology* 25:419–422. doi:10.1130/0091-7613
 640 Castruccio A, Rust AC, Sparks RJS (2013) Evolution of crust- and core-dominated lava
 641 flows using scaling analysis. *Bull Volcanol* 75:681. doi:10.1007/s004455-012-
 642 0681-2
 643 Crisp JA, Baloga SM (1990) A model for lava flows with two thermal components. *J*
 644 *Geophys Res* 95:1255–1270
 645 Crown DA, Baloga SM (1999) Pahoehoe toe dimensions morphology, and branching
 646 relationships at Mauna Ulu, Kilauea Volcano, Hawai‘i. *Bull Volcanol* 61:288–305
 647 Danes ZF (1972) Dynamics of lava flows *J Geophys Res* 77:1430–1432
 648 Doane DP (1976) Aesthetic frequency classifications. *American Statistician* 30:181–1905
 649 Dragoni M, Bonafede M, Boschi E (1986) Downslope models of a Bingham liquid:
 650 implications for lava flow. *J Volcanol and Geotherm Res* 30:305–325
 651 Day T, Muller JP (1989) Digital elevation model production by stereo-matching SPOT
 652 image-pairs: A comparison of algorithms. *Image Vision Comp* 7:95–101
 653 Gruen AW (1985) Adaptive least squares correlation: A powerful image matching
 654 technique. *S Afr J Photogramm Remote Sens Cartogr* 14:175–187
 655 Glaze LS, Baloga SM (2013) Simulation of inflated pahoehoe lava flows. *J*

656 Volcanol Geotherm Res, 255:108–123. doi:10.1016/j.jvolgeores.2013.01.018
 657 Guest JE, Wood C, Greeley R (1984) Lava tubes, terraces and megatumuli on the 1614–
 658 24 pahoe-hoe lava flow field, Mount Etna, Sicily. Bull Volcanol 47(3):635–648
 659 Hamilton CW, Thordarson T, Fagents SA (2010) Explosive lava–water interactions I:
 660 architecture and emplacement chronology of volcanic rootless cone groups in the
 661 1783–1784 Laki lava flow, Iceland. Bull Volcanol 72(4):449–467.
 662 doi:10.1007/s00445-009-0330-6.
 663 Harris AJL, Rowland SK (2001) FLOWGO: A kinematic thermo-rheological model for
 664 lava flowing in a channel. Bull Volcanol 63:20–44
 665 Harris AL, Dehn J, James MR, Hamilton C, Herd R, Lodato L, Steffke A(2007a)
 666 Pahoe-hoe flow cooling, discharge, and coverage rates from thermal image
 667 chronometry. Geophys Res Lett 34:L19303. doi:10.1029/2007GL030791
 668 Harris AJL, Dehn J, Calvari S(2007b) Lava effusion rate definition and measurement: a
 669 review. Bull Volcanol 70:1–22
 670 Harris AJL (2013) Lava flows. In: Modeling volcanic processes: the physics and
 671 mathematics of volcanism (eds. S.A. Fagents, T.K.P. Gregg, and R.M.C. Lopes).
 672 Cambridge Univ. Press, New York, pp 85–106
 673 Hon K, Kauahikaua J, Denlinger R, MacKay R (1994) Emplacement and inflation of
 674 pahe-hoe sheet flows: Observations and measurements of active lava flows on
 675 Kilauea Volcano, Hawaii. Geol Soc Am Bull 106:351–370
 676 Hoblitt RP, Orr TR, Heliker C, Denlinger RP, Hon K, Cervelli PF (2012) Inflation rates,
 677 rifts, and bands in a pāhoehoe sheet flow. Geosphere 8(5):179–195.
 678 doi:10.1130/GES00656.1

679 Hulme G (1974) The interpretation of lava flow morphology, *Geophys J R astr Soc*
 680 39:361–383
 681 Kauahikaua J, Cashman KV, Mattox TN, Heliker CC, Hon LA, Mangan MT, Thornber
 682 CR (1998) Observations on basaltic lava streams in tubes from Kilauea Volcano,
 683 island of Hawai'i. *J Geophys Res* 103(B11):27,303–27,323
 684 Keszthelyi L, Denlinger R (1996) The initial cooling of pahoehoe flow lobes. *Bull*
 685 *Volcanol* 58:5–18
 686 Keszthelyi L, Self S, Thordarson T (1999) Application of recent studies on the
 687 emplacement of basaltic lava flows to the Deccan Traps, *Memoirs – Geolog Soc*
 688 *India* 43:485–520
 689 Keszthelyi L, Self S, Thordarson T (2006) Flood lavas on Earth, Io and Mars. *J Geol Soc*
 690 163(2):253–264
 691 Keszthelyi L, McEwen AS, Thordarson T (2000) Terrestrial analogs and thermal models
 692 for Martian flood lavas. *J Geophys Res* 105(E6):15,027–15,049
 693 Kilburn CRJ (1996) Patterns and predictability in the emplacement of subaerial lava
 694 flows and flow fields. In: Scarpa R., R.I. Tilling (eds.) *Monitoring and mitigation*
 695 *of volcanic hazards*. Springer, New York: pp 491–537
 696 Koeppen WC, Patrick M, Orr T, Sutton AJ, Dow D, Wright R (2013) Constraints on the
 697 portioning of Kīlauea's lavas between surface and tube flows, estimated from
 698 infrared satellite data, sulfur dioxide emission rates, and field observations. *Bull*
 699 *Volcanol* 75:716. doi:10.1007/s00445-013-0716-3

700 Orr TR (2011) Lava tube shatter rings and their correlation with lava flux increases at
 701 Kīlauea Volcano, Hawai‘i. *Bull Volcanol* 73:355–346. doi:10.1007/s00445-010-
 702 0414-3
 703 Otto GP, Chau TKW (1989) Region-growing algorithm for matching of terrain images,
 704 *Image Vision Comp* 7:83–94
 705 Peitersen MN, Crown DA (2000) Correlations between topography and intraflow width
 706 behavior in Martian and terrestrial lava flows. *J Geophys Res* 105(E2):4123–4123
 707 Poland MP, Miklius A, Jeff Sutton A, Thornber CR (2012) A mantle-driven surge in
 708 magma supply to Kilauea Volcano during 2003–2007. *Nature Geosci* 5(4):295–
 709 300
 710 Ramsey MS, Harris AJL (2012) Volcanology 2010: How will thermal remote sensing of
 711 volcanic surface activity evolve over the next decade? *J Volcanol Geotherm Res.*
 712 249:217–233
 713 Resnick R, Halliday D (1977) *Physics: Part One* (3rd ed.). John Wiley & Sons, New York,
 714 608 p
 715 Robson S, James MR (2007) Photogrammetric image sequence processing to determine
 716 change in active lava flows. *Proc Remote Sensing and Photogrammetry Society*
 717 *Ann Conf, 2007 (RSPSoc 2007)*, 11–14th September, Newcastle upon Tyne, U.K.
 718 Rossi MJ, Gudmundsson A (1996) The morphology and formation of flow-lobe tumuli
 719 and Icelandic shield volcanoes. *J Volc Geotherm Res* 72:291–308
 720 Rowland SK, Harris AJL, Garbeil H (2004) Effects of martian conditions on numerically
 721 modeled, cooling-limited channelized lava flows. *J Geophys Res* 109(E10010).
 722 doi:10.1029/2004JE002288

723 Self S, Thordarson T, Keszthelyi L, Walker GPL, Hon K, Murphy MT, Long P,
 724 Finnemore D (1996) A new model for the emplacement of Columbia River
 725 basalts as large, inflated pahoehoe lava flow fields. *Geophys Res Lett* 23:2689–
 726 2692

727 Self S, Keszthelyi L, Thordarson T (1998) The importance of pāhoehoe. *Ann Rev Earth*
 728 *Planet Sci* 26(1):81–110

729 Smith WHF, Wessel P (1990) Gridding with continuous curvature splines in tension.
 730 *Geophysics* 55(3):293–305

731 Sturges H (1926) The choice of a class-interval. *J Amer Statist Assoc* 21:65–66

732 Thordarson T, Self S (1998) The Roza Member, Columbia River Basalt Group: A
 733 gigantic pahoehoe lava flow field formed by endogenous processes? *J Geophys*
 734 *Res* 103(B11):27411–27445

735 Walker GPL (1991) Structure, and origin by injection of lava under surface crust, of
 736 tumuli, 'lava rises', 'lava-rise pits', and 'lava-inflation clefts' in Hawaii. *Bull*
 737 *Volcanol* 53:546–558

738 Walker GPL (2009) The endogenous growth of pahoehoe lava lobes and morphology of
 739 lava-rise edges. In: Thordarson T, Self S, Larsen G, Rowland SK, Hoskuldsson A
 740 (eds) *Studies in volcanology—the legacy of George Walker* (Special Publications
 741 of IAVCEI No. 2). The Geol Soc: pp 17–32

742 Wilmoth RA, Walker GPL (1993) P-type and S-type pahoehoe: a study of vesicle
 743 distribution and patterns in Hawaiian lava flows. *J Volcanol Geotherm Res*
 744 55:129–142

Figures

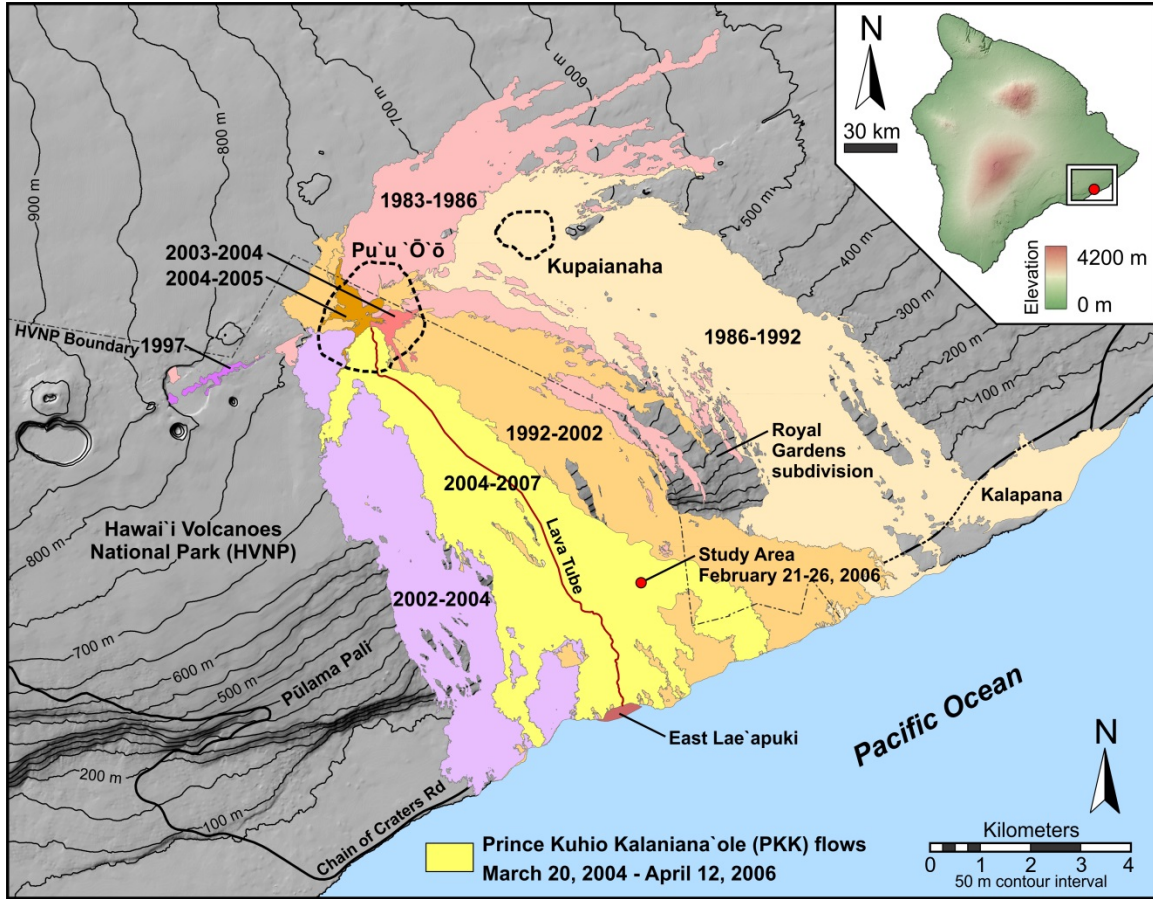


Figure 1. Lava flow map showing the study area location ($19.336430^{\circ}\text{N}$, $-155.055235^{\circ}\text{W}$) within the Prince Kūhiō Kalanianaʻole (PKK) flow (shown in yellow) on Kīlauea Volcano, Hawaiʻi. Pāhoehoe lava lobes at this locality were fed lava from Puʻu ʻŌʻō. Field measurements were acquired on 21–26 February 2006 for two lobes (A and B) located along the same lava pathway system. Lobe B was located directly down-slope of Lobe A, with a separation distance of ~ 10 m. The dashed lines approximately bound the edifices of Puʻu ʻŌʻō and Kupaianaha. Lava flow data provided by Tim Orr, United States Geologic Survey (USGS).

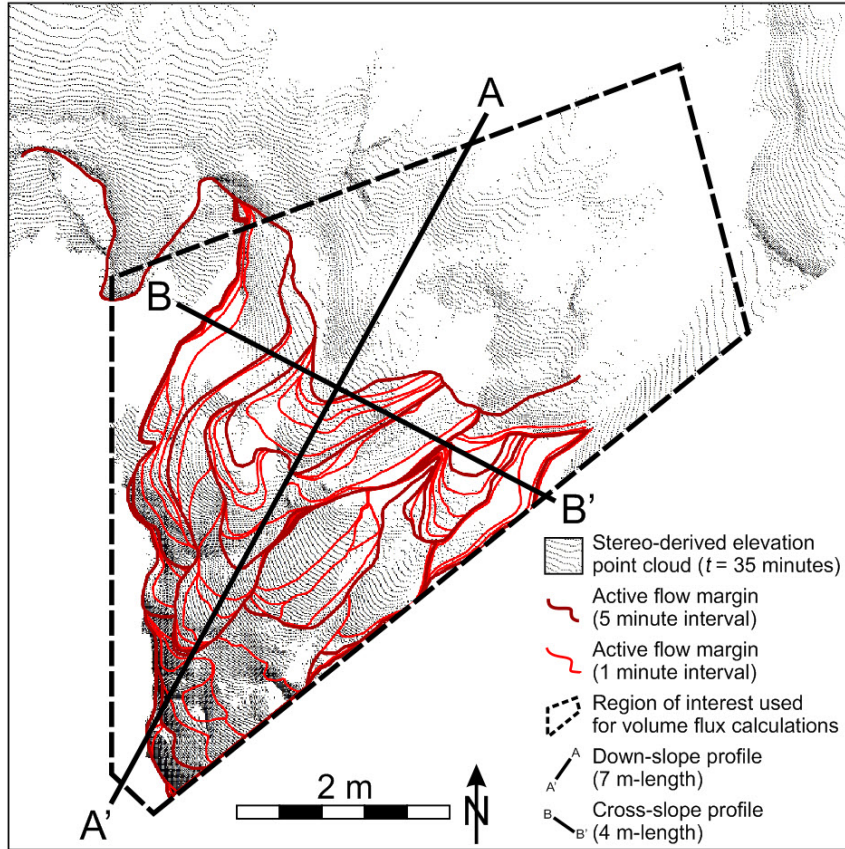
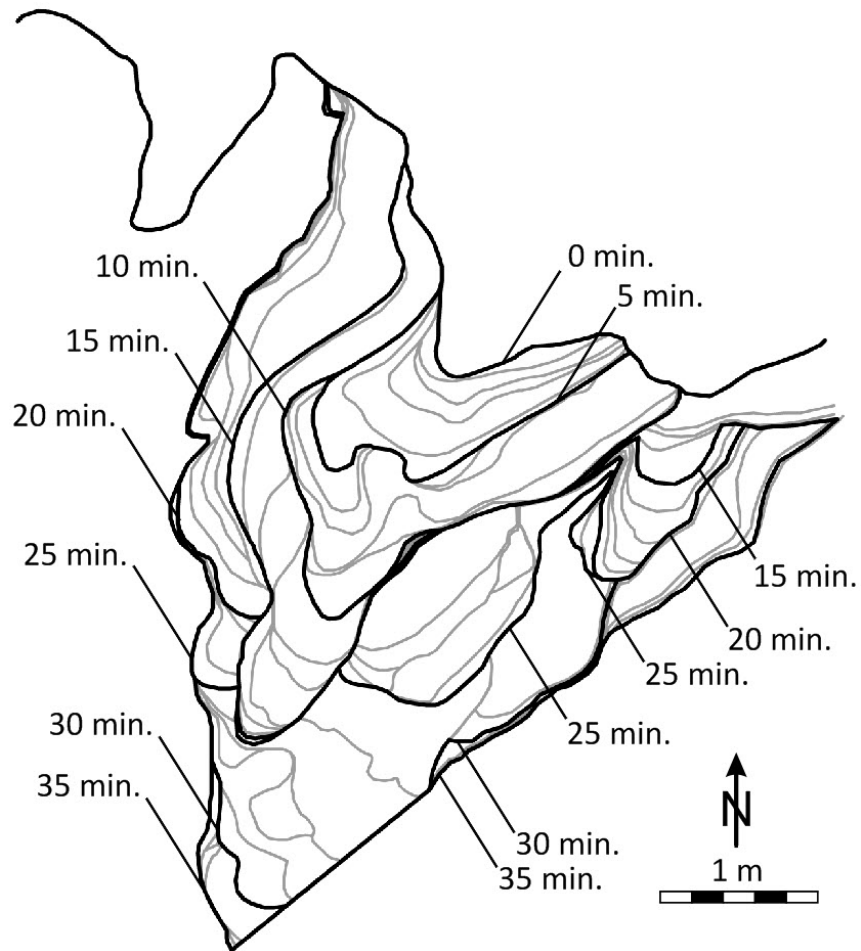


Figure 2. Orthorectified view of photogrammetric point cloud at time $t = 35$ minutes for Lobe A, with overlaid lava flow boundaries shown at 1 minute intervals and the locations of the down-slope ($\overline{AA'}$) and cross-slope ($\overline{BB'}$) profiles shown in Figure 4.



759

760 Figure 3. Time series evolution of Lobe A. Dark lines show the extent of the flow at 5
 761 minute intervals with grey lines showing the flow margins at 1 minute intervals. The flow
 762 begins to move outside the field of view at 28 minutes.

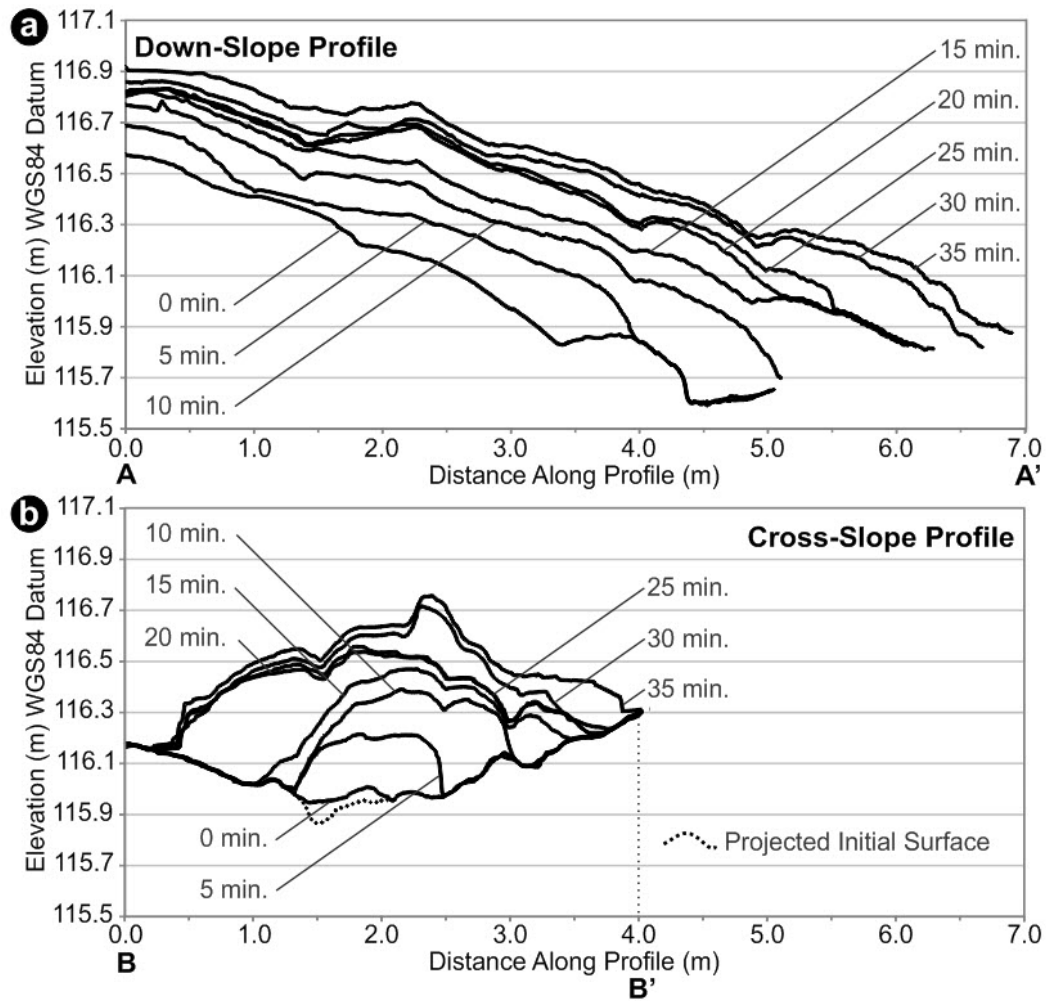


Figure 4. (a) Down-slope ($\overline{AA'}$) and (b) cross-slope ($\overline{BB'}$) profiles for Lobe A showing the changing topography of the lava lobe shown in Figures 1 and 2.

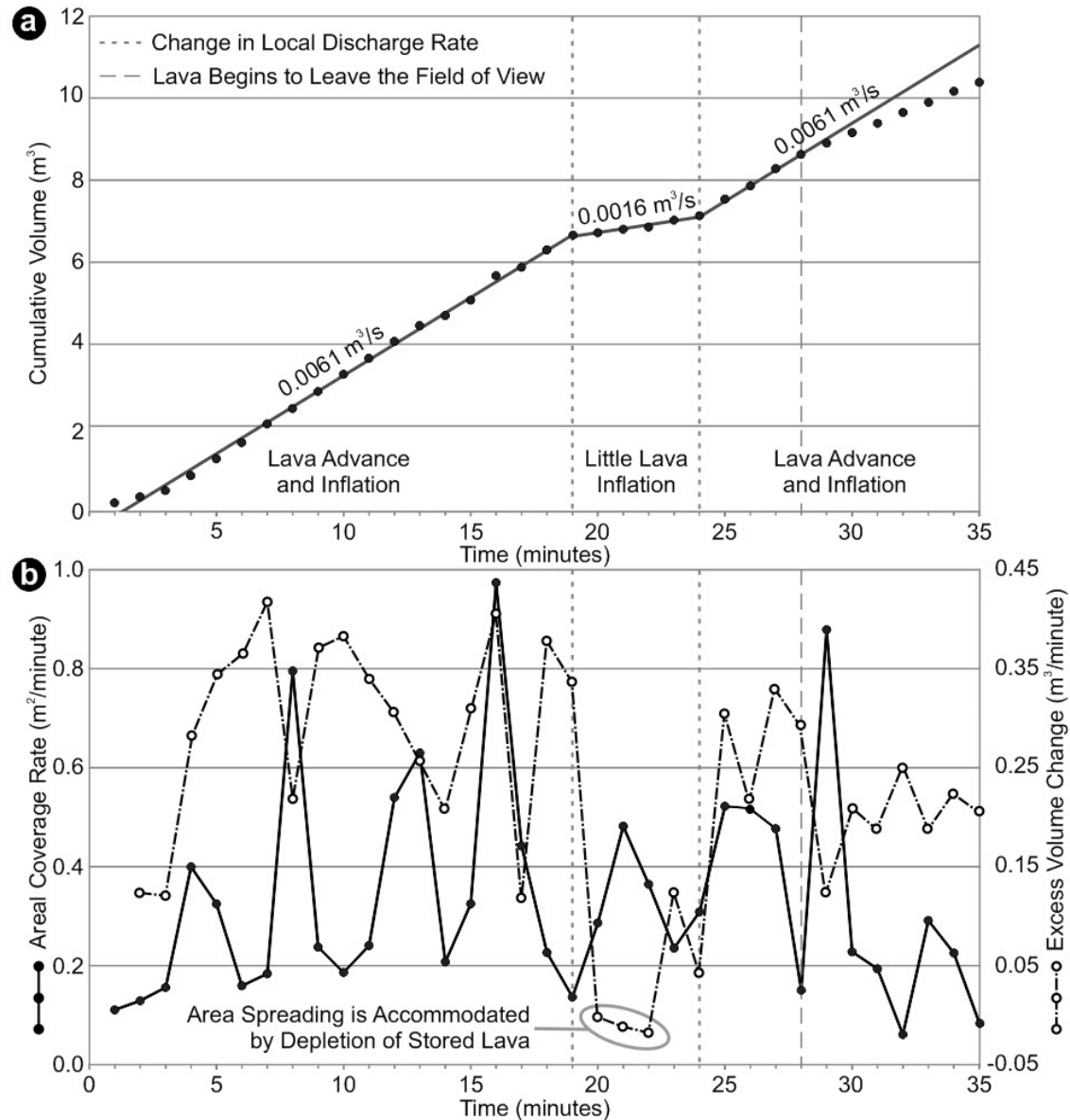


Figure 5. (a) Cumulative volume in the region of interest identified in Figure 2 for Lobe A. The mean local discharge rate ($0.0061 \pm 0.0019 \text{ m}^3 \text{s}^{-1}$, calculated for the first 19 minutes) is generally constant during the observation period, except for the interval between 19 and 24 minutes where the mean local discharge rate decreases by nearly a factor of four and the lobe experiences little inflation and generally lower than average areal spreading rates. At 28 minutes, the rate of volume change gradually decreases as the active flow front begins to exit the field of view of the stereo-cameras. (b) Areal coverage

774 rate (mean $0.33 \pm 0.23 \text{ m}^2/\text{minute}$, filled black circles with solid black line) and mean
775 excess volume change ($0.23 \pm 0.12 \text{ m}^3/\text{minute}$, open circles with broken line), where
776 excess volume change is defined in the text. Excess volume changes less than zero,
777 between 20–23 minutes, implies that areal growth was accommodated by depletion of
778 stored lava during this time interval. The areal coverage rate shows a periodicity with
779 peaks at intervals of 4.13 ± 0.64 minutes. All uncertainties are reported at 1σ .

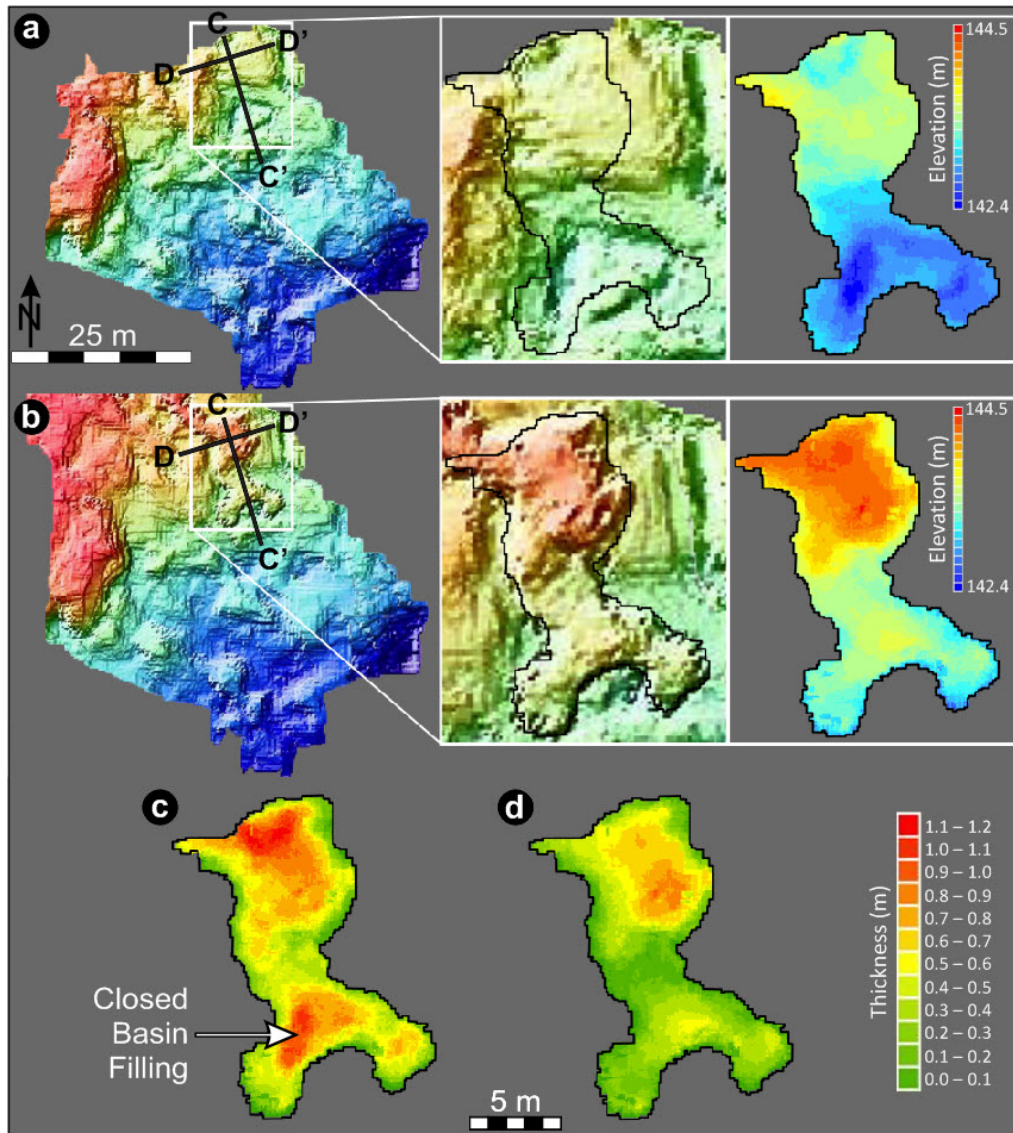


Figure 6. (a) Initial and (b) post-lava lobe emplacement digital terrain models (DTMs) generated from Differential Global Positioning System (DGPS) measurements for Lobe B, with cool colors showing low elevation and warm colors showing relatively higher elevation. (c) Simple difference between the final and initial topography. (d) Difference between the final topography and a Laplacian harmonic surface solution, which removes the effects of closed basin filling. Profiles $\overline{CC'}$ and $\overline{DD'}$ are shown in Figures 7a and 7b, respectively. Elevations in (a) and (b) are reported relative to the WGS84 datum, and lava thicknesses in (c) and (d) are shown to the same scale.

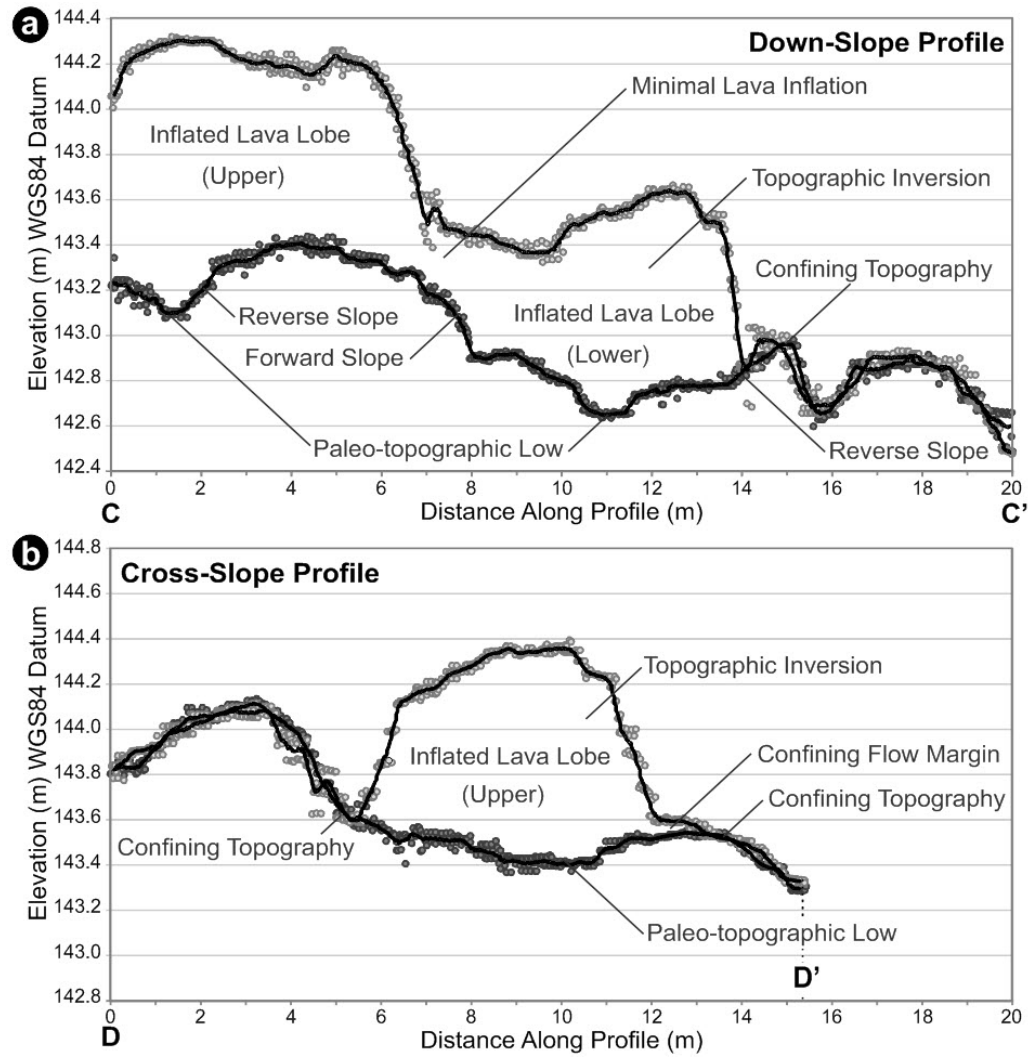


Figure 7. (a) Down-slope and (b) cross-slope profiles showing the initial and final topography for Lobe B (see $\overline{CC'}$ and $\overline{DD'}$ in Figure 6). The flow has topographically inverted the landscape, with inflation being greatest above paleo-topographic lows and anti-facing slopes, and least above forward-facing slopes. Note the pre-eruption topography and thin confining flow margins that may help to confine the thicker interior portions of the lobe.

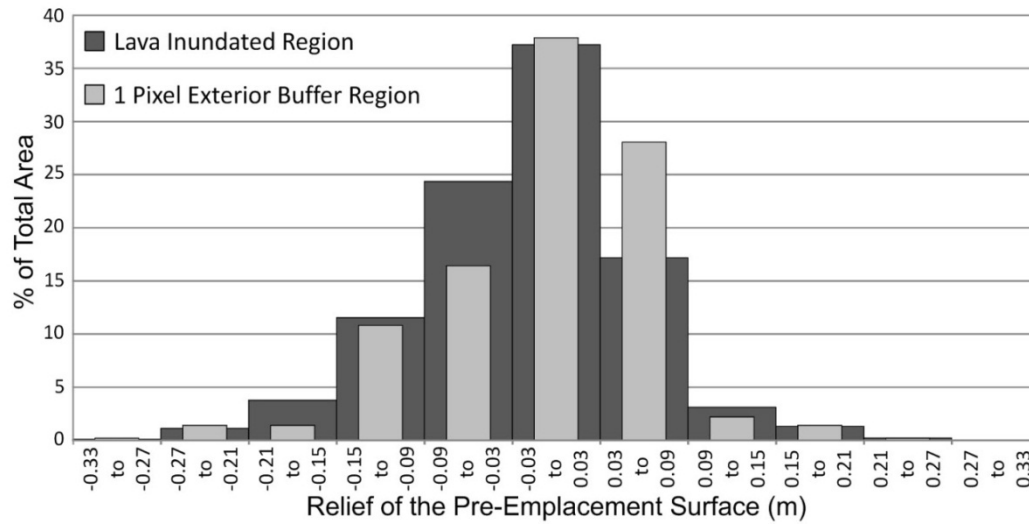


Figure 8. Frequency distribution of relief on initial surface within the lava inundated region (dark grey) and within a 1 pixel buffer region around Lobe B (light grey). The mean relief within both regions is close to zero (i.e., 0.02 ± 0.07 m in the inundated region and 0.00 ± 0.07 m in the buffer region), but the buffer region exhibits more +0.03 to +0.09 m relief surfaces and -0.09 to -0.03 m relief surface, which implies that positive relief on the order of only a few centimeters may act to confine the areal spreading of the flow. All uncertainties are reported at 1σ .

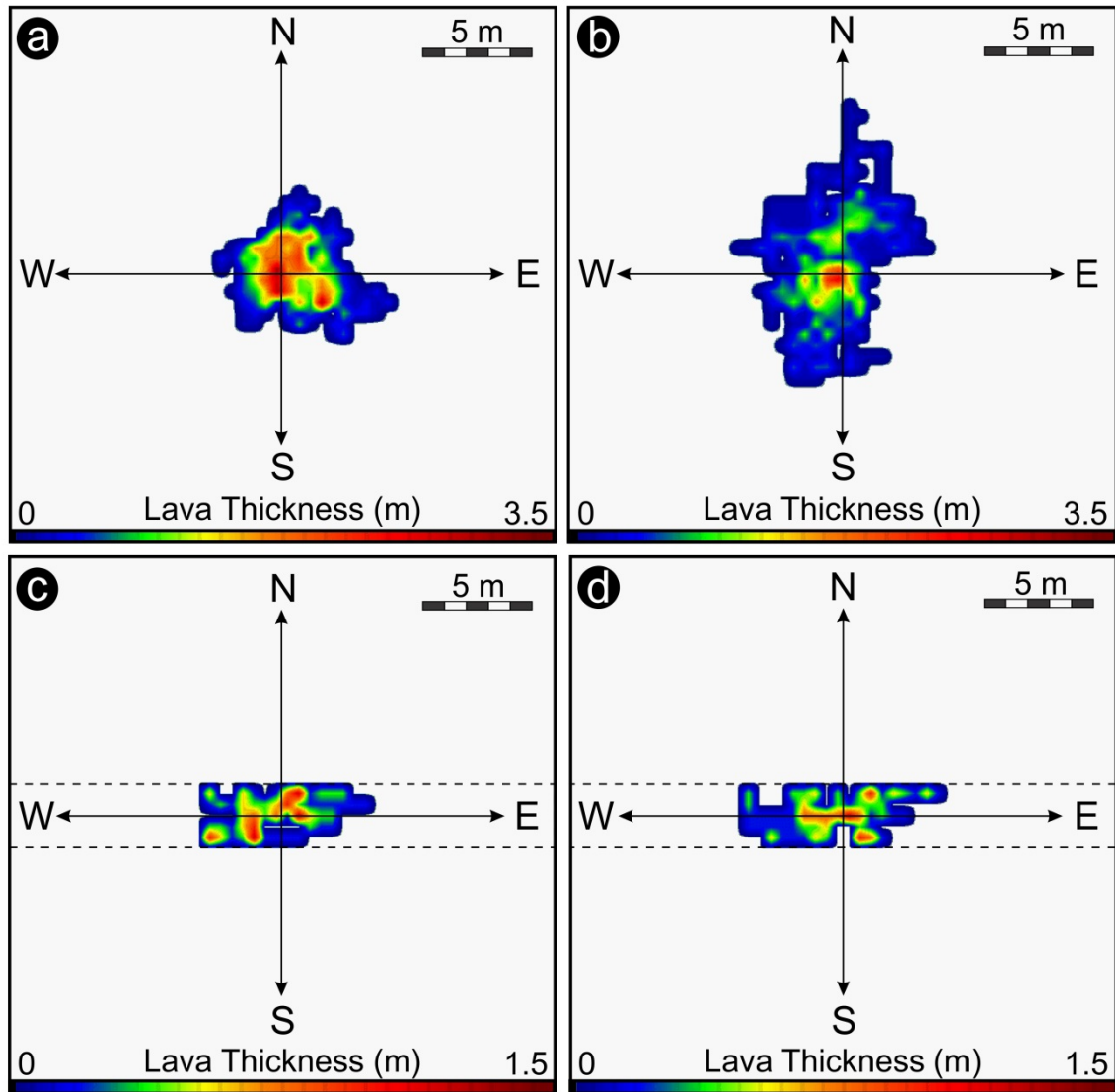


Figure 9. (a) Simulation of 500 randomly emplacement lava parcels (without sequential breakouts from lobe margins). The maximum flow thickness is 3.2 m. (b) Simulation of 500 lava parcels using the same probability distribution for correlated toe growth used to model Lobe A (i.e., $P(0) = P(1) = 0.25$ and $P(2) = 0.5$). The maximum flow thickness is 2.6 m. Note that including correlated breakouts in (b) increases the perimeter:area ratio relative to the random example shown in (a). (c and d) Plan view examples of two simulations of Lobe A using 117 lava parcels, boundaries (dash lines) at ± 3 cells on the North-South axis, and a probability distribution of $P(0) = P(1) = 0.25$ and

813 $P(2) = 0.5$ for adding 0, 1, and 2 extra parcels in the same direction when a parcel breaks
814 out from the flow margin. The maximum height of the flows shown in (c) and (d) are 1.2
815 m. For visualization purposes, the REBIN function in Interactive Data Language (IDL)
816 was used to magnify the cells by a factor of 10 and perform a default bilinear
817 interpolation. This process smoothes the model output and provides the exterior toes with
818 a rounded appearance. This process does not alter the raw model output shown in Figures
819 10 or 11b.

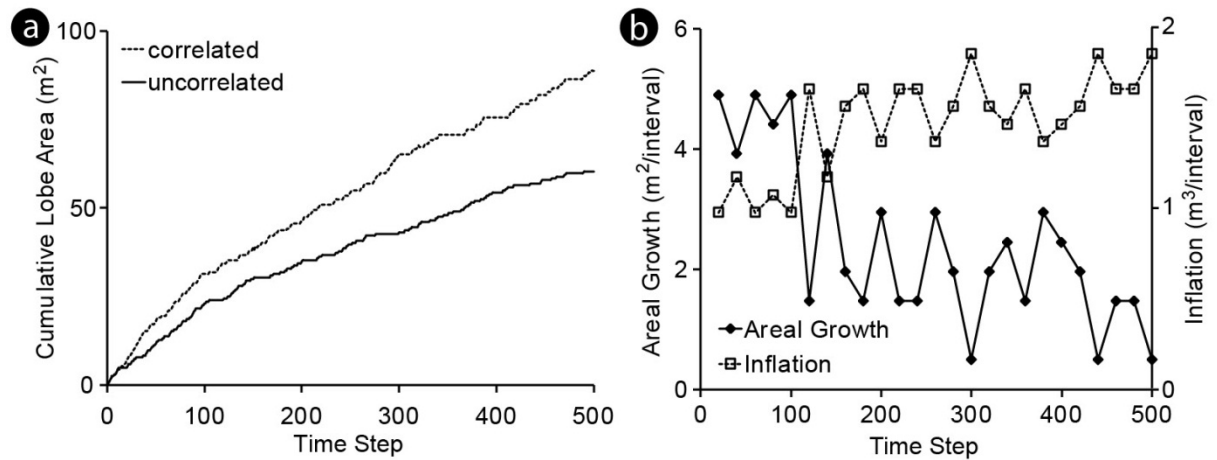


Figure 10. (a) Cumulative lobe area versus time for two stochastic simulation realizations of pāhoehoe lobe emplacement. The uncorrelated realization (lower solid line) was generated by considering purely random selection of both the location and direction of each parcel transfer. The correlated scenario (upper dashed line) modifies this model by introducing an increased probability of sequential parcel emplacement when new parcels break out at the periphery of the flow. In this case, the probabilities of adding 0, 1, and 2, correlated parcels are $P(0) = 0.25$, $P(1) = 0.25$, and $P(2) = 0.5$, respectively. (b) Shows the periodicities and anti-correlation in areal spreading and excess volume change for a typical purely random simulation and an interval of 20 time steps.

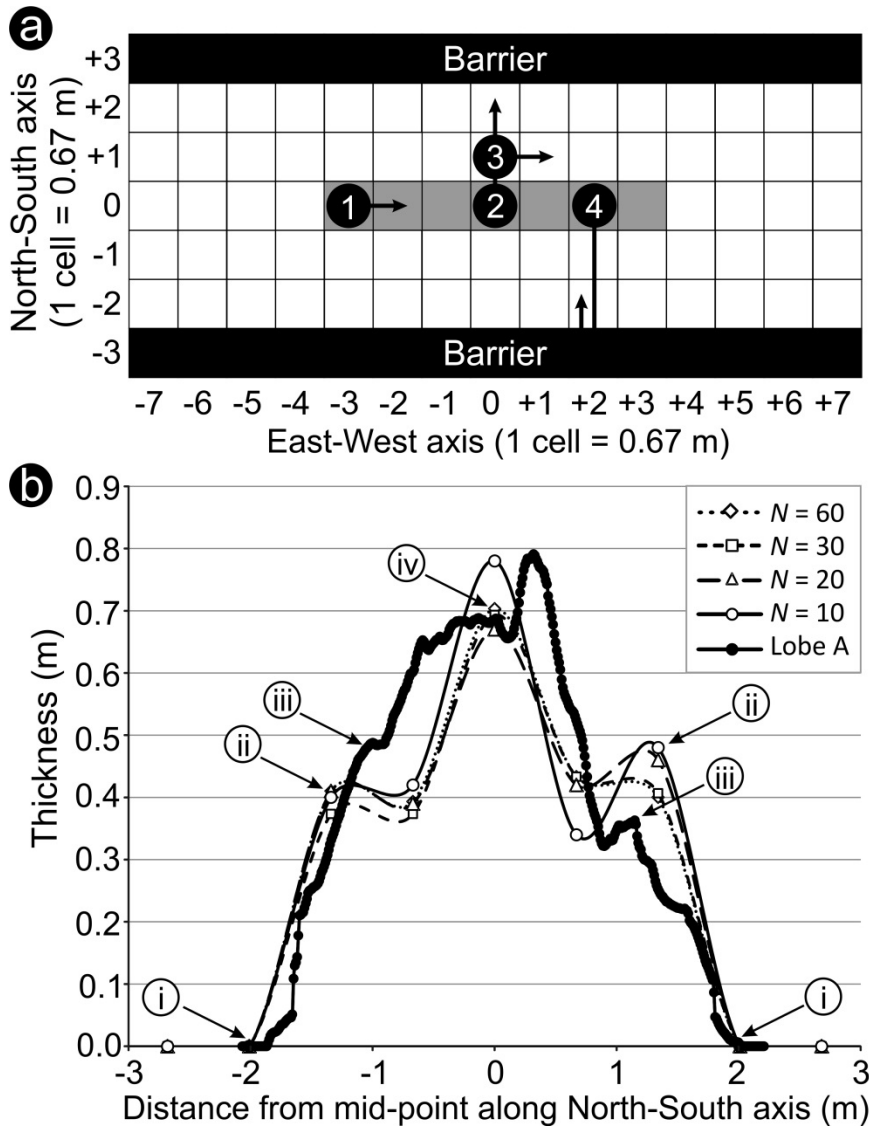


Figure 9. (a) A schematic example showing how the stochastic model works. A linear source region (shown in gray) passes through the mid-point of the array and trends East-West. Two parallel barriers are shown ± 3 cells from the linear source along the North-South axis. In the simulation, a cell is first chosen at random from within the confines of the flow (initially corresponding to the extent of the linear source region) and then a random cardinal direction is chosen. A lava parcel is then transferred to the specified cell (marked with a filled black circle, e.g., “1”) and to adjacent cell (identified by the associated arrow). If the parcel would be allocated beyond the confines of the flow, there

840 is a 0.25, 0.25, and 0.50 probability that 0, 1, or 2 extra parcels, respectively, will be
841 allocated to sequential cells in the same direction (e.g., “2” shows 1 extra, 2 total, cells
842 being added). As the areal extent of the flow increases, new parcel transfer locations
843 become available (e.g., “3”). If a cell allocation would result in a parcel being extended
844 beyond the barrier, then the parcel is reflected back towards the cell interior (e.g., “4”).
845 Each parcel allocated to a given cell increases its thickness by 0.2 m. This process is
846 repeated until all lava parcels are allocated, which in the case of Lobe A, includes a total
847 of 117 parcels. (b) Simulated North-South profiles for Lobe A, averaged over 10, 20, 30,
848 and 40 realizations of the model. The results show that despite the stochastic nature of the
849 model, the average simulations converge to a stable equilibrium shape over a few tens of
850 realizations. Also shown is the flow-perpendicular cross-section through Lobe A (Fig. 4b)
851 with the underlying topographic trend removed. “i”: The maximum width simulated lobes
852 and Lobe A are determined by the influences of topographic barriers. “ii”: Reflecting of
853 lava parcels by the barriers produces an excess thickening in the adjacent interior cells.
854 “iii”: High-standing topography and stagnated peripheral toes helps to confine the interior
855 of the lobe and promote inflation. “iv”: The thickest portion of the simulated lobe is
856 located along the medial axis and is generally consistent with the thickness of Lobe A
857 along the flow axis.